BAMS Article

Peering into Cloud Physics Using Ultra-Fine-Resolution Radar and Lidar Systems

Zeen Zhu,[a] Fan Yang,[a] Pavlos Kollias,[a,b] Katia Lamer,[a] Edward Luke,[a] James B. Mead,[d] Yong Meng Sua,[c] Andrew M. Vogelmann,[a] and Allison McComiskey[a]

KEYWORDS:
Cloud microphysics;
Clouds;
Lidars/Lidar observations;
Radars/Radar observations;
Remote sensing

ABSTRACT: Cloud microphysical processes, such as droplet activation, condensational growth, and collisional growth, play a central role in the evolution of clouds and precipitation. Accurate representations of these processes in numerical models are challenging partially due to incomplete understanding of them at the process level arising from limited systematic observations. Most surface-based active remote sensors, including today's operational cloud radars and lidars, have a resolution on the order of tens of meters. This resolution is insufficient to resolve cloud microphysical processes that manifest at finer (meter and submeter) scales. A new set of ultra-high-resolution ground-based radar and lidar systems have been developed to address this observational gap. The newly developed 94-GHz cloud radar has a range resolution down to 2.8 m, or a factor of 10 finer than typical radars, using a large bandwidth and quadratic phase coding techniques. The lidar has a range resolution down to 10 cm, or a factor of 100 finer than typical lidars, using a time-gated time-correlated single-photon-counting technique. Such high-resolution observations were previously only achievable through in situ aircraft measurements. Even then, aircraft measurements do not permit continuous long-term cloud observation as is possible with ground-based remote sensing instruments. In this study, the first-light cloud observations from the new radar and lidar systems are shown to reveal detailed cloud structures that conventional sensors could only perceive in a bulk sense, thus providing new avenues to investigate cloud microphysical processes and their impact on weather and climate.

SIGNIFICANCE STATEMENT: In this study, we introduced two novel remote sensing instruments capable of high-resolution cloud observations: a cloud radar system with a range resolution down to 2.8 m and a lidar system with a range resolution down to 10 cm. Observations show that the radar and lidar systems resolve detailed cloud structures and microphysical processes which would not be obtained from traditional remote sensing systems. The high-resolution measurements provide insights toward the understanding of cloud microphysics at a fundamental level.

DOI: 10.1175/BAMS-D-23-0032.1

Corresponding author: Zeen Zhu, zzhu1@bnl.gov

Publisher's Note: This article was modified on 26 February 2025 to correct the definition of the acronym "ACTRIS".

Manuscript received 19 February 2023, in final form 1 June 2024, accepted 15 July 2024

© 2024 American Meteorological Society. This published article is licensed under the terms of the default AMS reuse license. For information regarding reuse of this content and general copyright information, consult the AMS Copyright Policy (www.ametsoc.org/PUBSReuseLicenses).

Unauthenticated | Downloaded 06/03/25 05:57 PM UTC

AFFILIATIONS: [a] Brookhaven National Laboratory, Upton, New York; [b] Stony Brook University, State University of New York, Stony Brook, New York; [c] Stevens Institute of Technology, Hoboken, New Jersey; [d] ProSensing, Inc., Amherst, Massachusetts

1. Introduction

Clouds cover approximately two-thirds of Earth's surface at scales ranging from tens of meters to thousands of kilometers. Contrastingly, the fundamental physical mechanisms that control cloud formation and dissipation (e.g., cloud droplet activation and precipitation initiation) occur at scales down to micrometers (Yau and Rogers 1996). These fine-scale cloud processes are parameterized in regional and global models with much coarser resolutions, unavoidably leading to uncertainties in operational weather forecast and climate prediction (Suzuki et al. 2013; Zhu and Zhang 2006). Improvements in the representation of fine-scale cloud processes call for comprehensive and long-term high-resolution observations.

Measurements from active remote sensors such as lidar and millimeter-wavelength (cloud) radar have greatly contributed to improved understanding of the vertical distribution of clouds, aerosols, and precipitation at the global scale (Illingworth et al. 2015; Stephens et al. 2018). Furthermore, cloud radars and lidars are the centerpieces of surface-based observatories such as the U.S. Department of Energy (DOE) Atmospheric Radiation Measurement (ARM) observatories (Mather and Voyles 2013; Kollias et al. 2020) and the European Aerosols, Clouds and Trace Gases Research Infrastructure (ACTRIS) network which has its origin in the CloudNet project (Illingworth et al. 2007). These ground-based supersites provide continuous, long-term, and detailed observations of cloud and precipitation properties in the atmospheric column (Clothiaux et al. 2000; Kollias et al. 2007, 2016; Sassen 1991). Cloud radars utilize relatively (compared to precipitation radar) short wavelength to detect small cloud droplets and ice crystals and serve as a critical tool to characterize the internal structure of clouds and to investigate microphysical processes such as drizzle formation, secondary ice production, collision coalescence, riming, and aggregation (Kalesse et al. 2016; Kollias et al. 2011b; Luke et al. 2021; Vogl et al. 2022; Zhu et al. 2022). Lidars are more sensitive to high concentrations of aerosols and small cloud droplets and thus are commonly used for cloud-base detection, cloud-phase classification, and cloud number concentration retrieval (Liu et al. 2009; O'Connor et al. 2005; Wang and Sassen 2001; Wang et al. 2009). Lidars have also been used to characterize aerosol–cloud interactions and subcloud layer dynamical structures (Costantino and Bréon 2010; Lamer and Kollias 2015; Schmidt et al. 2015).

Over the last two decades, technological advancements have significantly improved the performance and sensitivity of cloud radars and lidars. However, one aspect that has practically remained unchanged is their range resolutions of commonly tens of meters. While this resolution is sufficient to resolve relatively large cloud structures such as generating cells (Keeler et al. 2016; Kumjian et al. 2014; Rauber et al. 2015), the melting layer (Fabry and Zawadzki 1995; Wolfensberger et al. 2016), and dynamical circulations in thick clouds (Rauber et al. 2017), it is insufficient to resolve much finer structures linked to cloud microphysical processes. For one, entrainment mixing plays a critical role in cumulus development (Krueger et al. 1997; Paluch and Baumgardner 1989; Warner 1973). Particularly, entrainment and mixing at cloud edges generate a cloudy–clear air interfacial

Unauthenticated | Downloaded 06/03/25 05:57 PM UTC

zone where cloud properties exhibit considerable variation within tens of meters (Pinsky and Khain 2019; Wood 2012), which cannot be explicitly resolved by current cloud radars due to their coarser resolutions.

It is thus anticipated that increasing the range resolution of radars and lidars resolves finer cloud structures that fundamentally enhance understanding of cloud microphysics close to the process level. However, developing and deploying high-resolution instruments is not without its challenges. For instance, there exists a fundamental dilemma between resolution and sensitivity in remote sensing instruments whereby detection sensitivity decreases with increasing resolution. This dilemma is one of the major obstacles to using high-resolution radars for atmospheric cloud research (Richards 2014). For a lidar system operating with a conventional photon-counting technique, range resolution is limited by the prescribed binning procedure and the instrument's data acquisition system's ability to collect large data amounts (Barton-Grimley 2019). These incompatible situations are mitigated, to some degree, by advancements in signal processing technology that have emerged during recent years. Nowadays, high-sensitivity cloud radar with meter-scale resolution and lidars with submeter-scale resolution are within reach (Barton-Grimley et al. 2018; Mead and Pazmany 2019; Pazmany and Haimov 2018).

In this article, new radar and lidar systems with high-resolution capability are introduced. The configurations and technologies being applied to these two instruments will be briefly introduced. Subsequent focus will be placed on the first-light observations containing unprecedented fine-scale cloud structures resolved by the high-resolution instruments along with their potential implication toward an improved understanding of cloud microphysics.

2. CMAS fixed observatory and instruments

The Brookhaven National Laboratory (BNL) Center for Multiscale Applied Sensing (CMAS; https://www.bnl.gov/cmas/) established a ground-based atmospheric observational facility (40.8656°N–72.8815°W, 25 m above mean sea level). It hosts an array of off-the-shelf instruments for atmospheric sensing including a Vaisala ceilometer, a radiometrics microwave radiometer (MWR), a METEK Micro Rain Radar (MRR-Pro), an over-the-top (OTT) Parsivel^2 disdrometer, and an OTT Pluvio^2 rain gauge. All the instruments are positioned close to each other to maximize the collocation of their complementary measurements. The next subsections describe the unique high-resolution radar and lidar systems (Fig. 1) that are part of the instrument suite.

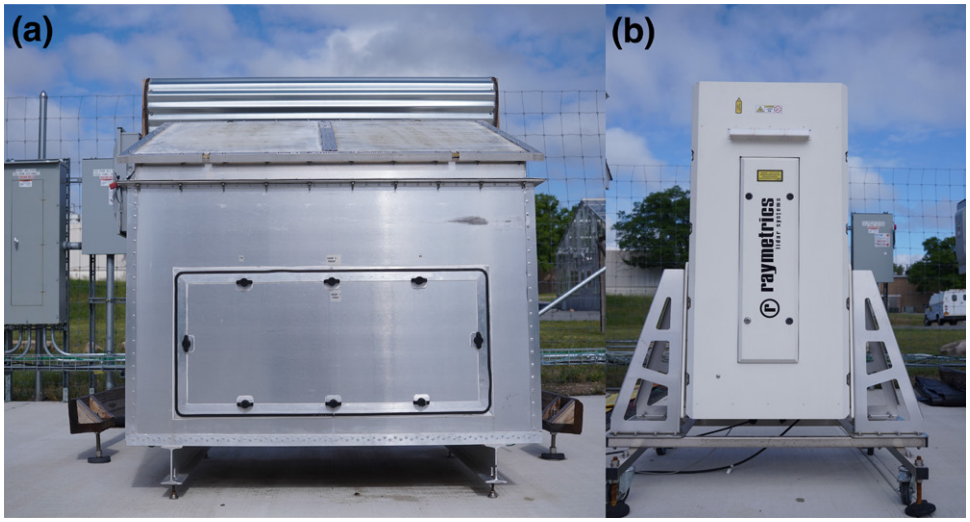

Fig. 1. Photo of the (a) WCR-QPC radar and (b) T2 lidar.

Unauthenticated | Downloaded 06/03/25 05:57 PM UTC

Table 1. Specifications of the WCR-QPC and T2 lidar.

WACR-QPC		T2 lidar	
Frequency	94.41 GHz	Wavelength	532 nm
Transmitter power	1 W	Output energy	~3.4 μJ
Antenna diameter	0.6 m	Receiver telescope aperture	~200 mm
Beamwidth	0.38°	Beam divergence	0.029 mrad
Range resolution	2.8–200 m	Minimum range resolution	~10 cm
Duty cycle	100%	Pulse repetition rate	20.6 kHz
Sensitivity at 1 km (at 30-m resolution, 2-s integration time)	−36 dBZ	Polarization	Linear
		Detector time resolution	45 ps
Sensitivity at 1 km (at 3-m resolution, 2-s integration time)	−22 dBZ	Pulse width	650 ps
		Maximum range	~7.28 km

a. High-resolution radar. The quadratic phase coded (QPC) W-band cloud radar (WCR-QPC) is a ground-based vertically pointing radar built by ProSensing (Mead and Pazmany 2019). The QPC technique allows the radar to transmit sinusoidal signals with quadratic phase increments between pulses. The received signal is decoded to align phases and processed via a single discrete Fourier transform (DFT), providing simultaneous velocity and range discrimination without needing the corner-turning memory in traditional radars. WCR-QPC is a single polarization radar, and it has separate transmit and receive antennae which allows operation at 100% duty cycle. The antennas are aligned to within 0.1° by separately finding the peak response of each antenna with a source placed 20 m from the radio frequency (RF) unit (J. Mead 2024, personal communication). The range resolution of the radar is adjustable from 2.8 to 200 m. Customized observational strategies are achieved by adjusting the range resolution, fast Fourier transform (FFT) length, maximum range, and integration time according to the cloud/precipitation system of interest. For instance, to detect fine structures near cloud top, a high-resolution mode is preferable with a longer integration time to compensate for reduced radar sensitivity. Some key specifications of the WCR-QPC for nominal operations are listed in Table 1. It is noted that the radar sensitivity shown in Table 1 applies to a 1-km distance. As sensitivity decreases with height, a lower sensitivity will occur at a higher altitude. As such, in this study, the WCR-QPC will be applied to detect boundary layer clouds and shallow precipitation systems.

The WCR-QPC measures radar Doppler spectra along with the first three moments, i.e., reflectivity, Doppler velocity, and spectrum width. Radar reflectivity is calibrated following the procedure detailed in Kollias et al. (2019). For a selected precipitation period, the "ground truth" reflectivity is estimated from disdrometer-observed drop size distributions (DSDs) using spherical particle (Mie theory) scattering calculations. This value is compared against the radar reflectivity observed at 100-m height while considering attenuation by liquid hydrometeors along this path.

b. High-resolution lidar. The time-gated time-correlated single-photon-counting lidar (named the T2 lidar) was built by Raymetrics Inc. and Stevens Institute of Technology under the guidance of atmospheric scientists at Brookhaven National Laboratory. It is a 532-nm wavelength ground-based lidar that achieves a range resolution down to 10 cm by applying the time-correlated single-photon-counting (TCSPC) technique, instead of the multichannel scaler technique that is widely applied in existing atmospheric profiling lidars (Campbell et al. 2002). It can operate in the time-gated mode, in which the T2 lidar only receives backscattered photons in a small time-gated window [details in Yang et al. (2023b)]. (Brief introductions to the multichannel scaler technique and time-correlated single photon counting

Unauthenticated | Downloaded 06/03/25 05:57 PM UTC

Photon-counting techniques

Multichannel scalers

Photon-counting lidars are widely used for cloud and aerosol observations. For conventional profiling lidars, the photon acquisition technique (Fig. SB1) commonly used is based on multichannel scalers, where the number of detected photons is recorded in preallocated time intervals which correspond to lidar range resolution. The received photon numbers at each time are accumulated during a given period, corresponding to the lidar temporal resolution, to generate the photon waveform from which the backscatter is estimated.

TCSPC

With the TCSPC technique, the lidar records the arrival time of each photon relative to the most recently emitted laser pulse. The lidar range resolution is limited by the laser pulse width, which at 650 ps is down to about 10 cm (Barton-Grimley et al. 2018; Yang et al. 2023b). The received time sequence of photons within a given period is binned to generate a signal waveform. This technique provides the flexibility for the lidar to have customized range resolutions to investigate specific cloud regions of interest.

TCSPC with a time-gated mode

The T2 lidar with the TCSPC and time-gated technique observes a small region by setting the delay time η, after which the detector window is opened following each laser pulse, and the width of the gated window τ, which is how long the detector is open. This technique allows the lidar to receive backscattered photons only within the time-gated window, which can be used to scan upward through a narrow cloud region at high-range resolution. A detailed description of the T2 lidar time-gated technique is given in Yang et al. (2023b).

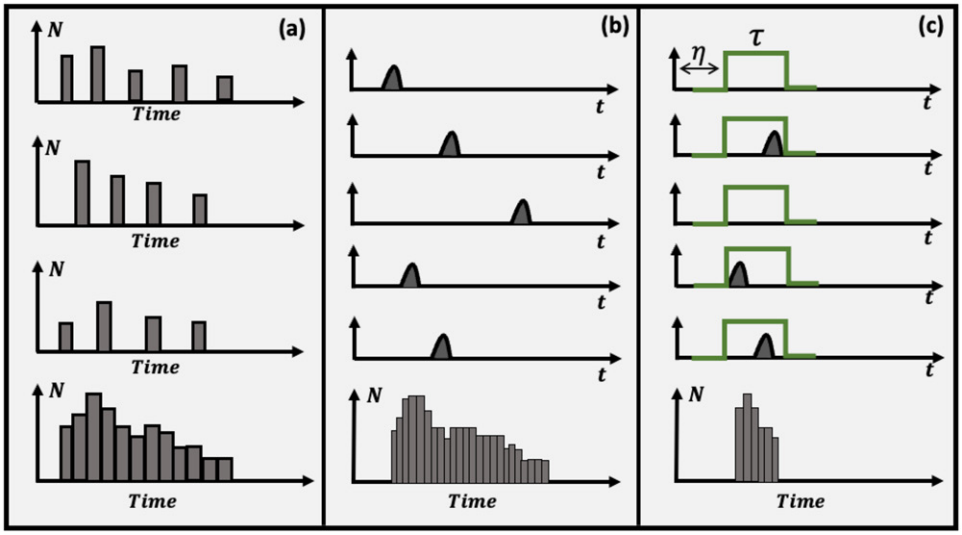

Fig. SB1. Schematic of the photon-counting technique with (a) multichannel scalers, (b) TCSPC, and (c) TCSPC with a time-gated mode. Panels (a) and (b) are modified from Becker (2005). The stacked plots are at different altitudes.

technique, as well as the time-gated technique, are presented in the "Photon counting techniques" sidebar.) The width of the time-gated window can be set as small as 5.5 ns corresponding to a range of 0.825 m and as large as 80 ns corresponding to a range of 12 m. The dead time of the T2 lidar detector is approximately 50 ns, which is close to the maximum width of the gated window. This means that in the time-gated mode, the detector is unlikely to receive more than one backscattered photon after each emitted laser pulse. Key specifications of the T2 lidar for nominal operations are listed in Table 1.

3. Fine cloud structures resolved by the WCR-QPC and the T2 lidar

One unique capability of remote sensing instruments is their providing vertically resolved cloud structure. The extent to which the structure is resolved is dependent upon the range

Unauthenticated | Downloaded 06/03/25 05:57 PM UTC

resolution of the sensor. To highlight the benefits of high-resolution observations, we conducted close comparison experiments by applying the WCR-QPC and T2 lidar to detect various cloud regions using different range resolutions.

a. Cloud-base structure. For actively developing clouds, cloud base is the height where aerosols in the subcloud layer are activated into cloud particles under supersaturation driven by updrafts. The hydrometer and dynamic properties near cloud base are of great importance. In models, the updraft mass flux at cloud base is essential for developing cumulus parameterizations (Grant 2001; Lamer et al. 2015; Sakradzija and Hohenegger 2017), and an accurate determination of cloud-base height is also crucial to retrieving liquid water content and cloud droplet number concentration from remote sensing observations (Snider et al. 2017; Vivekanandan et al. 2020; Zhu et al. 2019). Several theoretical studies have developed estimates of cloud-base height from surface measurements (Bolton 1980; Lawrence 2005; Romps 2017) which need accurate cloud-base observations for validation. However, cloud-base heights detected from traditional lidar instruments do not agree well with each other and have uncertainties on the order of tens of meters due to their intrinsic range resolution and the nebulous nature of applying a human label (i.e., cloud base height) to a continuously developing process (Martucci et al. 2010; Wang et al. 2018). Recent laboratory studies indicate that supersaturation fluctuations caused by small-scale turbulence play an important role in the activation of droplets and their subsequent growth (Prabhakaran et al. 2020). Thus, it is anticipated that cloud-base height might fluctuate in the presence of strong turbulence near cloud base. The T2 lidar with its range resolution down to 10 cm has the capability to discern fine cloud-base structures and provide accurate cloud-base measurements needed to assess theoretical estimates and reduce cloud retrieval uncertainty.

Figure 2 demonstrates the ability of the T2 lidar to resolve fine cloud-base structure compared with the ceilometer. The vertically pointing ceilometer outputs backscatter β profiles at a range resolution of 10 m every 30 s (Fig. 2a). The T2 lidar, operating in the time-gated mode, scans the cloud-base region as illustrated in Fig. 2b: (i) A 12-m time-gated window is applied below cloud base to receive photons within the window for 1 s; (ii) the gated window is subsequently moved upward by 1.5 m for another 1 s of observation; and (iii) this process continues until the gated window reaches the altitude where the received backscattered photons are reduced significantly due to attenuation.

During the observation period, the ceilometer observes a cloud with base near 1.67 km where the backscatter intensity is greatly enhanced (Fig. 2c). Figure 2d illustrates the cloud-base structure detected from the ceilometer at 2031:04 local time where, starting around 1.66 km, the backscattered intensity rapidly increases to its peak value at 1.70 km, showing a 40-m transition zone. As the range resolution of the ceilometer is 10 m, the observed four range gates are insufficient to depict a detailed process in the transition region. To further probe the structure within this 40-m distance, five time-gated sampling profiles observed from the T2 lidar are shown for the lowest 18 m of this region (Fig. 2e). Through the 10-cm resolution measurements, we find that the peaks of the profiles vary within 10 m (i.e., from 1.67 to 1.68 km) during the 5-s observational period, showing the highly fluctuating characteristics of cloud microphysics in the cloud-base region. Furthermore, the five profiles shown in Fig. 2e exhibit distinct shapes, with the number of photons received peaking toward the lower part of the gated window as the window enters the cloud layer. This feature links to fundamental microphysical processes within the subcloud region, which will be discussed later in this paper. Overall, the T2 lidar with its high temporal/range resolution provides unique observations with which to investigate the finely resolved cloud-base structure and the associated cloud processes.

Unauthenticated | Downloaded 06/03/25 05:57 PM UTC

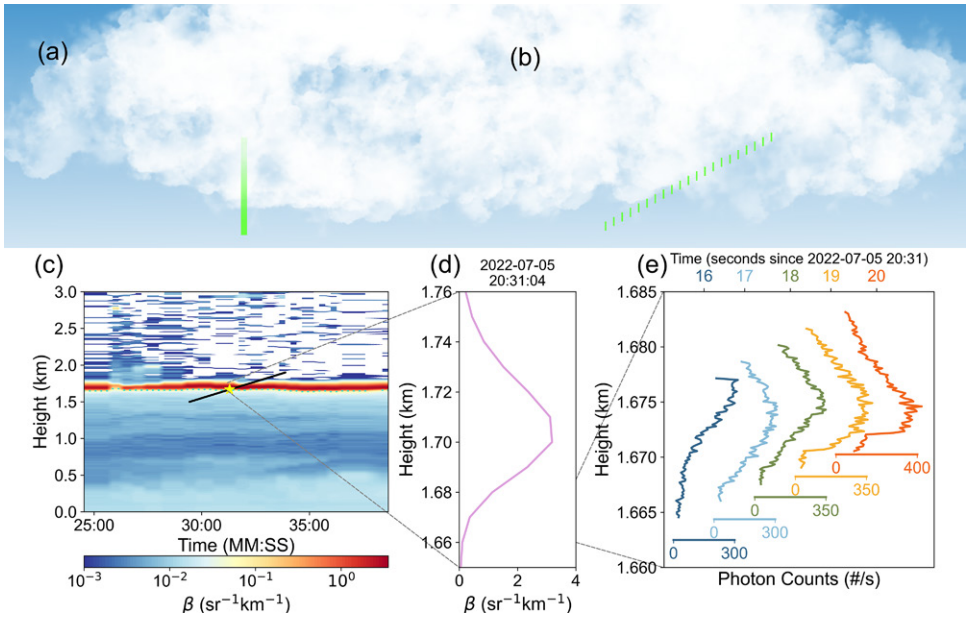

Fig. 2. Schematic of the sampling strategy for the (a) ceilometer and (b) T2 lidar operated in the time-gated mode. The ceilometer produces a backscatter profile, while the T2 lidar only receives backscattered photons within the time-gated window. The T2 lidar scans the cloud-base region as shown in (b) and detailed in the text. (c) Backscatter profiles observed from ceilometer on 5 Jul 2022, at the CMAS site. The slanted solid black line indicates the scanning region of the T2 lidar. (d) A close-up view of the ceilometer-observed backscatter profile near cloud base observed at 2031:04 LT [shown as the yellow star in (c)]. (e) Profiles of backscattered photons observed by the T2 lidar in five gated windows near cloud base. Each colored profile indicates one second of observations from the T2 lidar in the time-gated window between 2031:16 and 2031:20 LT.

b. Internal cloud structure. Inside the cloud, interactions of microphysical and dynamical processes commonly manifest as unique cloud internal structures. For instance, from the cloud radar perspective, drizzling stratocumulus exhibits a typical structure where radar reflectivity increases toward cloud base due to the development of drizzle particles (Kollias et al. 2011b; Wood 2012), and unique Doppler spectrum skewness patterns can be identified inside cloud for stratocumulus with or without virga beneath cloud base (Luke and Kollias 2013). In this study, to highlight the advantage of using high-resolution radar to resolve internal cloud structure, we will focus on a thin liquid water cloud occurring within the boundary layer. Leahy et al. (2012) defined optically thin clouds as the subset of marine low clouds that do not fully attenuate lidar signals. Optically thin clouds constitute about half of the low-level clouds over the marine domain and cover 28% of the globe (Leahy et al. 2012). Due to their extensive coverage, thin clouds contribute significantly to the planetary albedo and subsequently modulate Earth's radiative energy budget (Bennartz et al. 2013). However, the macro- and microphysical properties of thin liquid clouds are not fully understood due to observational limitations. For instance, large discrepancies in retrieved cloud properties exist among different retrieval methods for clouds with liquid water paths lower than 100 g m^{-2} (Turner et al. 2007). A space-borne lidar with a range resolution of 60 m overestimates thin cloud thickness with uncertainty as large as 100% (Leahy et al. 2012). Thus, increasing the radar range resolution enhances the observational capability of thin liquid water clouds and provides additional constraints that may serve to reduce cloud retrieval uncertainty (Zhu et al. 2019).

An example of a thin cloud layer observed by the WCR-QPC is shown in Fig. 3. We first operate the WCR-QPC at a range resolution of 30 m, which is commonly utilized in other ground-based cloud radars (Kollias et al. 2016). For this configuration, the cloud layer with 120-m thickness is resolved only by four range gates (left column of Fig. 3).

Unauthenticated | Downloaded 06/03/25 05:57 PM UTC

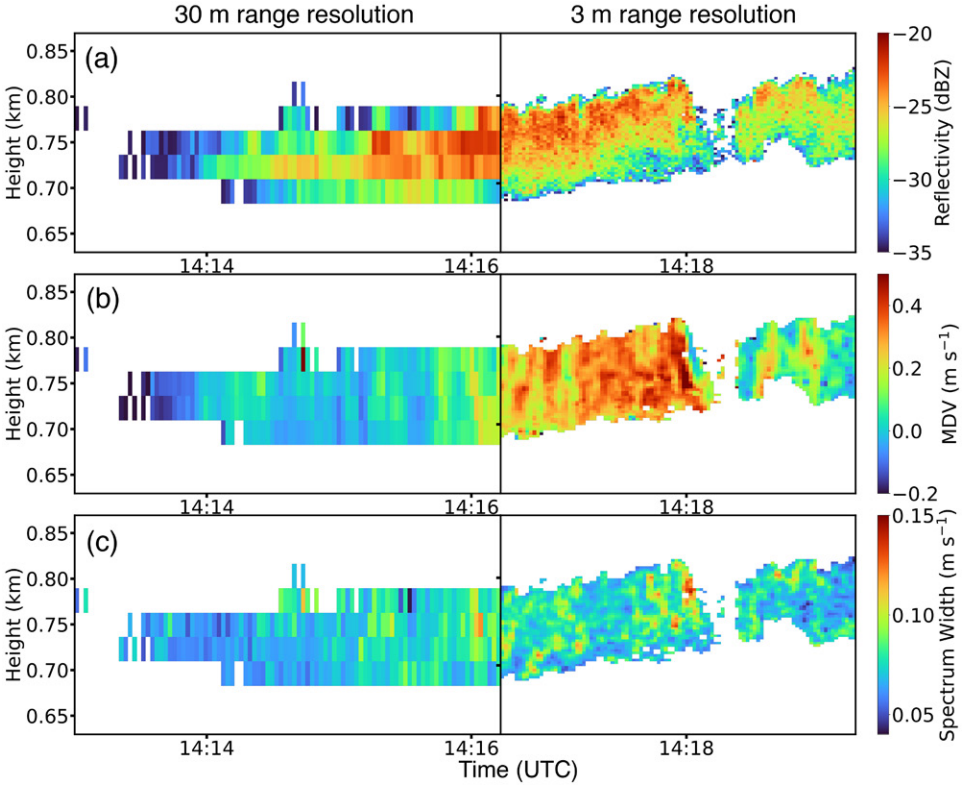

Fig. 3. (a) Reflectivity, (b) mean Doppler velocity (MDV), and (c) spectrum width for a thin cloud layer observed by the WCR-QPC at the CMAS Observatory on 1 Nov 2022. Two range resolutions are applied during the observational period: (left) observed at 30-m range resolution; (right) observed at 3-m resolution.

Such low-resolution measurements are insufficient to depict the in-cloud structure, making it challenging to investigate detailed cloud processes. In contrast, when using 3-m range resolution (right column of Fig. 3), the cloud internal structure and the associated dynamical characteristics are more explicitly resolved. From cloud base to top, radar reflectivity consistently increases until a rapid reduction of −8 dBZ occurs within two range gates (~6 m) near cloud top at around 0.8 km. The increase in reflectivity toward cloud top indicates condensational growth of cloud droplets, which is supported by the continuous upward motion of ~0.4 m s^{-1} within the cloud layer (Fig. 3b). The reflectivity pattern of this thin cloud layer is different from typical drizzling stratocumulus clouds, for which the largest reflectivity occurs near cloud base due to the presence of large drizzle drops (Kollias et al. 2011b). Here, the reflectivity pattern indicates that collision coalescence is inefficient. An enhanced spectrum width region is shown at 1418 UTC (Fig. 3c), from 0.75 to 0.80 km, which is consistent with the wind shear characteristics shown in the Doppler velocity field (Fig. 3b). In general, the spectrum width within this cloud layer is lower than 0.15 m s^{-1} (Fig. 3c), suggesting a relatively nonturbulent environment.

c. Cloud-top structure. Cloud top is another region where fundamental cloud processes, such as droplet formation, dissipation, and precipitation initiation, occur (Khain and Pinsky 2018; Small and Chuang 2008). It is widely recognized that the structure near cloud top is extremely complicated due to the intertwined processes of entrainment mixing, radiative and evaporative cooling, and cloud microphysics (Mellado 2017). To investigate the complex processes occurring near cloud top, large-eddy simulation (LES) with meter-scale resolution is commonly applied (Moeng et al. 2005; Yamaguchi and Randall 2012). While such investigating framework is readily achieved in LES, it is not readily achievable within an observational study. To resolve the cloud-top structure, radar measurements with meter-scale

Unauthenticated | Downloaded 06/03/25 05:57 PM UTC

resolution are a must. Here, we present a unique example showing the detailed cloud-top structure resolved from the WCR-QPC observations.

Figure 4 shows a cloud-top region of a shallow precipitating system observed by the WCR-QPC using fine-range (3 m) and coarse-range (30 m) resolutions. With the 3-m resolution, distinctive dynamic structures near cloud top are identifiable, where updraft plumes rise from the main cloud body at 0.85 km (Fig. 4b). These uprising plumes are also identifiable in the radar reflectivity field (Fig. 4a), but with much lower reflectivity compared to the cloud below 0.85 km. The reduced reflectivity suggests the existence of dry air surrounding the uprising plumes leading to evaporation. Another interesting feature to note in Fig. 4b is the strips of downward motion embedded between the upward plumes. These up/downdraft motions contribute to an enhanced turbulence region as shown by the large spectrum widths in Fig. 4c. A large turbulent region near cloud top plays an important role in the evolution of the cloud system and the formation of precipitation (Grabowski and Wang 2013; Magaritz-Ronen et al. 2016; Prabhakaran et al. 2020; Shaw 2003). In contrast, the cloud top resolved from the 30-m resolution is relatively flat without showing fluctuating characteristics; individual updraft/downdraft plumes are washed out, and the spectrum widths are higher than from the 3-m resolution observations. Comparing the two sets of measurements demonstrates that the high-resolution radar resolves detailed cloud-top structure and has the potential to promote scientific discovery. For instance, the updraft plumes present "generating cell (GC)" structures which are commonly found in large-scale stratiform precipitation systems but are rarely documented in warm shallow precipitation. These plumes are approximately 300 m wide and 200 m deep, which are narrower than the generating cells that occur at the top of stratiform clouds (Keeler et al. 2016). Similar small-scale GCs are also observed in the shallow cloud system over the Southern Ocean (Wang et al. 2020), echoing the existence of a much narrow GC structure than previously measured.

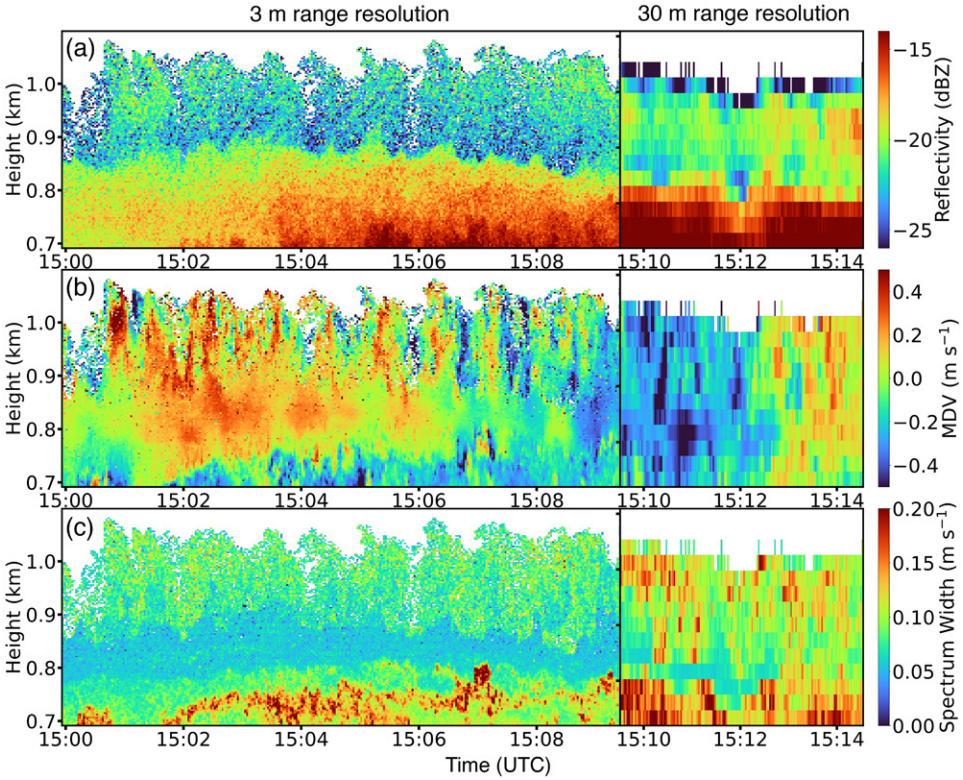

Fig. 4. (a) Reflectivity, (b) MDV, and (c) spectrum width at cloud top for a shallow precipitating system observed by the WCR-QPC at the CMAS Observatory on 1 Nov 2022. Different range resolutions are applied for the observational period: (left) 3-m range resolution; (right) 30-m resolution.

Unauthenticated | Downloaded 06/03/25 05:57 PM UTC

4. Detailed microphysical features resolved from WCR-QPC and T2 lidar

A fundamental task in cloud microphysics is to understand the formation and development of clouds and precipitation (Yau and Rogers 1996). For example, the mechanism that triggers rain initiation is not well understood. Particularly, our current understanding of droplet growth by diffusion (i.e., the process controlling cloud droplet growth) and collision coalescence (i.e., the process controlling raindrop growth) is insufficient to explain the ubiquitousness of drizzle particles that exist in warm clouds (Wang and Grabowski 2009; Yang et al. 2018; Zhu et al. 2022). Moreover, cloud microphysical processes are further modulated by aerosols and aerosol–cloud interactions which are the largest forcing uncertainty in anthropogenic climate change (IPCC 2023, 2021). To this end, fine-scale cloud measurements from the high-resolution radar/lidar system provide new insights toward understanding of cloud microphysics and its impact on weather and climate.

a. Warm rain formation. The Doppler spectrum observed from vertical-pointing cloud radar has proved to be a valuable tool for probing cloud microphysical processes (Kollias et al. 2011a). Specifically, the Doppler spectrum records the received backscattered power as a function of Doppler velocity and provides information on hydrometeor sizes/types under prevailing dynamical conditions. Large particles have faster fall velocities and larger backscattered powers than their smaller counterparts. These characteristics manifest as unique Doppler spectrum signatures that can be used as fingerprints to identify cloud microphysical features. For instance, the third moment of the Doppler spectrum, the Doppler skewness, is commonly used to identify drizzle particles and to investigate drizzle initiation (Acquistapace et al. 2017; Kollias et al. 2011b; Zhu et al. 2022). Likewise, in mixed-phase clouds, liquid droplets and ice crystals have different fall velocities, generating Doppler spectra with multimodes, a feature that is widely used for cloud-phase classification and identification of different ice-growth mechanisms (Kalesse et al. 2016; Luke et al. 2021; Shupe et al. 2004; Vogl et al. 2022). Nevertheless, there are two limitations in cloud radar measurements that severely hinder the interpretation of microphysics from Doppler spectra. First, cloud microphysical processes develop rapidly based on individual particles on scales of several millimeters down to micrometers. Conventional radar volumes typically constitute hundreds to thousands of cubic meters, for which tens of billions of particles jointly contribute to the radar received power. In this case, any distinct microphysical features within a small region are averaged out, resulting in a smooth Doppler spectrum. A second limitation is due to the Doppler spectrum broadening by turbulence. Turbulence sampled within a large radar volume causes broadening that smooths out the Doppler spectrum, making the microphysical features less pronounced (Zhu et al. 2023) (An illustration of the turbulence-broadening effect on the Doppler spectrum is shown in the "How range resolution affects the Doppler spectrum" sidebar.) These two limitations are mitigated to a degree by the application of high-resolution cloud radar. The following example is used to demonstrate the benefits of applying WCR-QPC to identify detailed cloud microphysical processes that would be inaccessible to conventional cloud radar.

Figure 5 shows observations of a warm precipitating cloud collected by the WCR-QPC over a 1-h period at 3-m range resolution. Over the observation period, cyclical variations were recorded in cloud-top height, varying from 1.2 to 1.8 km of altitude. The cloud-top region also has areas with large spectrum widths beginning around 1430 UTC (Fig. 5c). While spectrum width is affected by a range of factors (see Sidebar 2 for more details), this signature is generally consistent with the presence of strong turbulence. Figure 5d shows 10 Doppler spectra collected within a 30-m profile located in the black square in Figs. 5a–c. Differing Doppler spectra morphologies are identifiable within this small region. Doppler spectra at the upper levels have two distinctive peaks separated by a narrow valley. This signature is consistent with the presence of two hydrometeor populations with slightly different fall

Unauthenticated | Downloaded 06/03/25 05:57 PM UTC

How radar range resolution affects the Doppler spectrum

For a vertical-pointing cloud radar, the Doppler spectrum width σ has contributions from the spread of the DSD σ_d, wind shear σ_s, and turbulence σ_t (Borque et al. 2016):

$$\sigma^2 = \sigma_d^2 + \sigma_s^2 + \sigma_t^2,$$

where σ_t is dependent upon the radar observation volume and manifests as a lower σ_t in a smaller radar volume for a given turbulent environment. A theoretical estimation of σ_t for two different resolutions (3 and 30 m) is shown in Fig. SB2a: At 1-km height, σ_t is 0.15 m s^{-1} with 3-m resolution and 0.27 m s^{-1} with 30-m resolution. The difference in σ_t strongly affects the radar Doppler spectrum morphology. An example is shown in Fig. SB2c for the same DSD shown in Fig. SB2b: Three peaks and two valleys are identifiable in the Doppler spectrum with σ_t = 0.15 m s^{-1} (blue line), indicating detailed cloud microphysical features therein, while a Doppler spectrum with σ_t = 0.27 m s^{-1} (yellow line) has a smoother morphology.

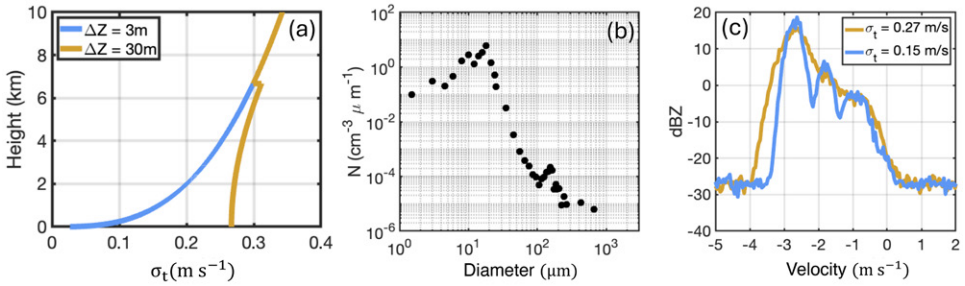

Fig. SB2. (a) Estimated σ_t for 3- and 30-m radar range resolutions for, following Borque et al. (2016), an environmental eddy dissipation rate of 5 × 10^{-3} m^2 s^{-3} and radar beamwidth of 0.3°. (b) In situ observed DSD for a drizzling cloud measured during the Aerosol and Cloud Experiments in the Eastern North Atlantic (ACE-ENA) field campaign (Wang et al. 2022). (c) Simulated Doppler spectrum for the DSD shown in (b) for different σ_t values: The blue line represents a σ_t of 0.15 m s^{-1} corresponding to range resolution of 3 m, and the yellow line represents a σ_t of 0.27 m s^{-1} corresponding to range resolution of 30 m. The approach to simulating the Doppler spectrum is from Kollias et al. (2011a).

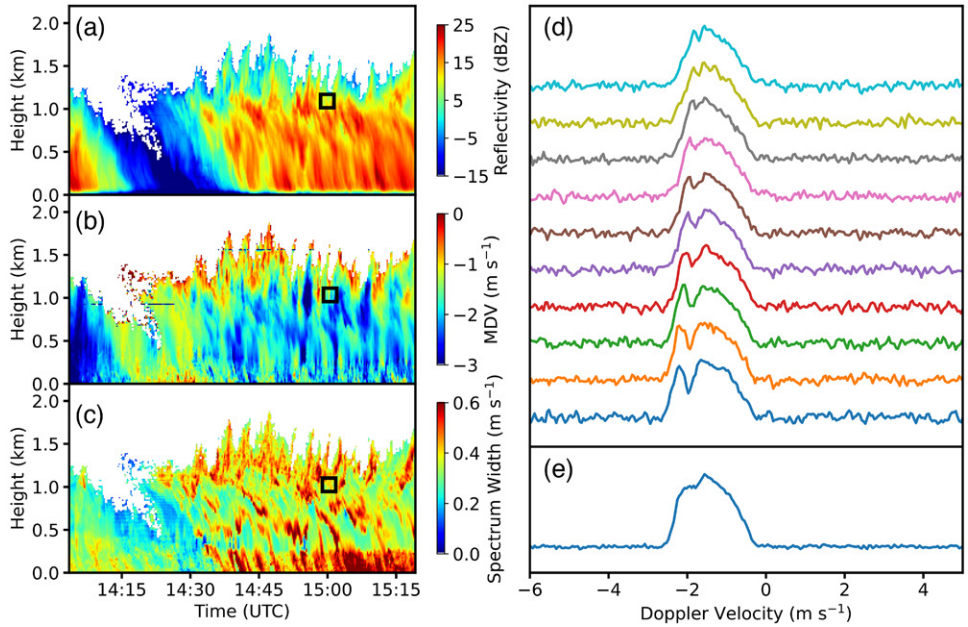

Fig. 5. Observations from the WCR-QPC at 3-m range resolution during a warm-phase precipitation event on 2 May 2022: (a) radar reflectivity, (b) MDV, and (c) spectrum width. Negative (positive) velocity in (b) and (d) represents downward (upward) motions. (d) Doppler spectra within the region indicated by the black box in (a)–(c) collected at 3-m range resolution. (e) The average of the 10 spectra illustrated in (d), thereby representing the corresponding spectrum at 30-m resolution. In (d), the spectra are offset for clarity.

Unauthenticated | Downloaded 06/03/25 05:57 PM UTC

speeds. Doppler spectra at lower levels also show two peaks, but they are more separated in velocity with a much deeper valley separating them. This again suggests the presence of two hydrometeor populations but with a larger difference in fall speed. The evolution of the Doppler spectra from the top to the bottom implicates the growth of drizzle droplets due to the collision coalescence. In contrast, the Doppler spectrum reconstructed for 30-m range resolution (Fig. 5e) has no clear bimodality. The lack of bimodality compared with 3-m resolution is due to two reasons. First, when averaged over 30 m, the fine-scale features shown in Fig. 5d that vary with height are smoothed out and are no longer visible. Second, with a coarser-range resolution, the Doppler spectrum is more affected by turbulence, which will also smooth out the spectrum and conceal distinctive features that are visible in the high-resolution measurements.

b. Aerosol–cloud interactions. Aerosol–cloud interactions (ACIs) are widely recognized as the largest forcing uncertainty in climate models (Fan et al. 2016). Specifically, the focus of ACI is to understand how increased aerosol loading due to anthropogenic or natural emissions affects cloud properties (IPCC 2023). One key process related to ACI is the formation of cloud droplets from aerosol particles, which is commonly investigated using laboratory experiments, in situ aircraft measurements, and numerical simulations (Chen et al. 2016; Prenni et al. 2007; Wang et al. 2008). Current remote sensing instruments are inadequate to investigate droplet activation processes because the processes occur within a meter or less of cloud base, which is challenging to observe using lidar with a resolution of tens of meters. Instead, the T2 lidar with submeter resolution has the potential to provide a remote sensing–based perspective of cloud droplet activation.

The five profiles in Fig. 2e illustrate the subcloud layer resolved by the T2 lidar. Take the profile observed at 2031:16 local time (dark blue line) as an example. The lower half of the 12-m gated window shows a gradual increase in photons received with height, which is likely linked to the hygroscopic growth of haze particles below cloud base. The upper half of the window has a rapidly enhanced photon number, indicating the activation of cloud droplets. As the gated window moves upward into the cloud region, i.e., from 16 to 20 s, the peak in photon number shifts to the lower part in the gated window. The slopes of the photon profiles from the subcloud to cloudy regions increase rapidly from 16 to 20 s due to stronger backscatter by cloud droplets than the smaller haze particles. Consequently, the photon distribution within time-gated windows manifests fine cloud microphysical features. This unique set of observations opens a new observational approach to tackle unsolved issues in cloud droplet activation (Yang et al. 2024). Recent modeling has indicated that the interactions of haze particles with cloud droplets may have a strong impact on cloud properties (Hoffmann et al. 2022; Yang et al. 2023a). With the T2 lidar, the activation and growth of haze particles are expected to be resolved, providing a promising capability to improve understanding of cloud droplet activation in the context of ACI.

5. Conclusions and outlook

Conventional cloud radars with resolutions of tens of meters depict detailed in-cloud structures compared to weather radars with resolutions of hundreds of meters. Nonetheless, cloud radars are unable to detect fine-scale cloud structures related to fundamental microphysical processes, especially for those that occur in the cloudy boundary layer. Many of these structures are particularly poorly understood and represented in models. To improve upon current observational capabilities, we introduce a set of radar and lidar systems that use novel technologies to achieve ultra-high-range resolution down to submeter scale, which is up to two orders of magnitude finer than the current cloud remote sensing instruments.

Unauthenticated | Downloaded 06/03/25 05:57 PM UTC

First-light observations of the high-resolution radar and lidar systems reveal a detailed view of fine cloud structures and microphysical features that exist within a variety of cloud systems. Particularly, the high-resolution observations are invaluable for the investigation of important structures exhibited within thin cloud layers and near cloud boundaries. From the T2 lidar, observations near the cloud-base region reflect the vertical development of a cloud, revealing droplet activation and condensational growth. Radar with 3-m range resolution depicts intricate structures near cloud top, indicating that the entrainment mixing process has the potential to be observed at a new level of detail. Furthermore, a smaller radar sampling volume enables the detection of Doppler spectra with multimode features, which allows distinctive cloud microphysical characteristics to be identified and interpreted. We anticipate application of the high-resolution remote sensing observations will bring new observational perspectives to the cloud physical community for addressing the most urgent cloud problems.

With the continuous advancement of remote sensing technology, observational limits of cloud sensing capability can be extended. For instance, rapidly evolving submillimeter radar technology is enabling range resolutions down to centimeter magnitude (Cooper and Chattopadhyay 2014). At centimeter-scale resolution, radar observations are well matched with in situ measurements, further closing the gap between remote sensing and in situ probes (Zhu et al. 2024). Radars with centimeter resolution enable the feasibility of their application in laboratory facilities such as a large cloud chamber to provide nonintrusive observations (Shaw et al. 2020; Zhu et al. 2024). Utilizing the T2 lidar, the highly resolved vertical profile of backscattered photons enables remote estimation of cloud droplet concentration, providing critical information for understanding aerosol–cloud interactions (Yang et al. 2024). These upcoming high-resolution instruments, along with their new observational strategies, offer new observational opportunities to improve understanding of cloud microphysical processes at a fundamental level.

Acknowledgments. Funding support for the WCR-QPC and the T2 lidar was provided by Brookhaven National Laboratory via the Laboratory Directed Research and Development Grants LDRD 22-054 and 21-039.

Data availability statement. Several datasets are available at the data portals for the SBU-BNL Radar Observatory (http://radarscience.weebly.com). The high-resolution radar/lidar data presented in this study are available upon request.

Unauthenticated | Downloaded 06/03/25 05:57 PM UTC

References

Acquistapace, C., S. Kneifel, U. Löhnert, P. Kollias, M. Maahn, and M. Bauer-Pfundstein, 2017: Optimizing observations of drizzle onset with millimeter-wavelength radars. *Atmos. Meas. Tech.*, **10**, 1783–1802, https://doi.org/10.5194/amt-10-1783-2017.

Barton-Grimley, R. A., 2019: Single photon counting lidar techniques and instrumentation for geoscience applications. University of Colorado at Boulder, 265 pp., https://www.proquest.com/openview/c783d7280d030a06d05b74e2a24176e4/1?pq-origsite=gscholar&cbl=18750&diss=y.

——, R. A. Stillwell, and J. P. Thayer, 2018: High resolution photon time-tagging lidar for atmospheric point cloud generation. *Opt. Express*, **26**, 26 030–26 044, https://doi.org/10.1364/OE.26.026030.

Becker, W., 2005: *Advanced Time-Correlated Single Photon Counting Techniques.* Vol. 81. Springer Science & Business Media, 401 pp.

Bennartz, R., and Coauthors, 2013: July 2012 Greenland melt extent enhanced by low-level liquid clouds. *Nature*, **496**, 83–86, https://doi.org/10.1038/nature12002.

Bolton, D., 1980: The computation of equivalent potential temperature. *Mon. Wea. Rev.*, **108**, 1046–1053, https://doi.org/10.1175/1520-0493(1980)108<1046:TCOEPT>2.0.CO;2.

Borque, P., E. Luke, and P. Kollias, 2016: On the unified estimation of turbulence eddy dissipation rate using Doppler cloud radars and lidars. *J. Geophys. Res. Atmos.*, **121**, 5972–5989, https://doi.org/10.1002/2015JD024543.

Campbell, J. R., D. L. Hlavka, E. J. Welton, C. J. Flynn, D. D. Turner, J. D. Spinhirne, V. S. Scott III, and I. H. Hwang, 2002: Full-time, eye-safe cloud and aerosol lidar observation at atmospheric radiation measurement program sites: Instruments and data processing. *J. Atmos. Oceanic Technol.*, **19**, 431–442, https://doi.org/10.1175/1520-0426(2002)019<0431:FTESCA>2.0.CO;2.

Chen, J., Y. Liu, M. Zhang, and Y. Peng, 2016: New understanding and quantification of the regime dependence of aerosol-cloud interaction for studying aerosol indirect effects. *Geophys. Res. Lett.*, **43**, 1780–1787, https://doi.org/10.1002/2016GL067683.

Clothiaux, E. E., T. P. Ackerman, G. G. Mace, K. P. Moran, R. T. Marchand, M. A. Miller, and B. E. Martner, 2000: Objective determination of cloud heights and radar reflectivities using a combination of active remote sensors at the ARM CART sites. *J. Appl. Meteor.*, **39**, 645–665, https://doi.org/10.1175/1520-0450(2000)039<0645:ODOCHA>2.0.CO;2.

Cooper, K. B., and G. Chattopadhyay, 2014: Submillimeter-wave radar: Solid-state system design and applications. *IEEE Microwave Mag.*, **15**, 51–67, https://doi.org/10.1109/MMM.2014.2356092.

Costantino, L., and F.-M. Bréon, 2010: Analysis of aerosol-cloud interaction from multi-sensor satellite observations. *Geophys. Res. Lett.*, **37**, L11801, https://doi.org/10.1029/2009GL041828.

Fabry, F., and I. Zawadzki, 1995: Long-term radar observations of the melting layer of precipitation and their interpretation. *J. Atmos. Sci.*, **52**, 838–851, https://doi.org/10.1175/1520-0469(1995)052<0838:LTROOT>2.0.CO;2.

Fan, J., Y. Wang, D. Rosenfeld, and X. Liu, 2016: Review of aerosol–cloud interactions: Mechanisms, significance, and challenges. *J. Atmos. Sci.*, **73**, 4221–4252, https://doi.org/10.1175/JAS-D-16-0037.1.

Grabowski, W. W., and L.-P. Wang, 2013: Growth of cloud droplets in a turbulent environment. *Annu. Rev. Fluid Mech.*, **45**, 293–324, https://doi.org/10.1146/annurev-fluid-011212-140750.

Grant, A. L. M., 2001: Cloud-base fluxes in the cumulus-capped boundary layer. *Quart. J. Roy. Meteor. Soc.*, **127**, 407–421, https://doi.org/10.1002/qj.49712757209.

Hoffmann, F., B. Mayer, and G. Feingold, 2022: A parameterization of interstitial aerosol extinction and its application to marine cloud brightening. *J. Atmos. Sci.*, **79**, 2849–2862, https://doi.org/10.1175/JAS-D-22-0047.1.

Illingworth, A. J., and Coauthors, 2007: Cloudnet: Continuous evaluation of cloud profiles in seven operational models using ground-based observations. *Bull. Amer. Meteor. Soc.*, **88**, 883–898, https://doi.org/10.1175/BAMS-8-6-883.

——, and Coauthors, 2015: The EarthCARE satellite: The next step forward in global measurements of clouds, aerosols, precipitation, and radiation. *Bull. Amer. Meteor. Soc.*, **96**, 1311–1332, https://doi.org/10.1175/BAMS-D-12-00227.1.

IPCC, 2021: *Climate Change 2021: The Physical Science Basis*. IPCC, 2 pp.

——, 2023: Summary for Policymakers: Synthesis report of the IPCC sixth Assessment Report (AR6): Longer report. IPCC, 1–36.

Kalesse, H., W. Szyrmer, S. Kneifel, P. Kollias, and E. Luke, 2016: Fingerprints of a riming event on cloud radar Doppler spectra: Observations and modeling. *Atmos. Chem. Phys.*, **16**, 2997–3012, https://doi.org/10.5194/acp-16-2997-2016.

Keeler, J. M., B. F. Jewett, R. M. Rauber, G. M. McFarquhar, R. M. Rasmussen, L. Xue, C. Liu, and G. Thompson, 2016: Dynamics of cloud-top generating cells in winter cyclones. Part I: Idealized simulations in the context of field observations. *J. Atmos. Sci.*, **73**, 1507–1527, https://doi.org/10.1175/JAS-D-15-0126.1.

Khain, A. P., and M. Pinsky, 2018: *Physical Processes in Clouds and Cloud Modeling.* Cambridge University Press, 626 pp.

Kollias, P., E. E. Clothiaux, M. A. Miller, B. A. Albrecht, G. L. Stephens, and T. P. Ackerman, 2007: Millimeter-wavelength radars: New frontier in atmospheric cloud and precipitation research. *Bull. Amer. Meteor. Soc.*, **88**, 1608–1624, https://doi.org/10.1175/BAMS-88-10-1608.

——, J. Rémillard, E. Luke, and W. Szyrmer, 2011a: Cloud radar Doppler spectra in drizzling stratiform clouds: 1. Forward modeling and remote sensing applications. *J. Geophys. Res.*, **116**, D13201, https://doi.org/10.1029/2010JD015237.

——, W. Szyrmer, J. Rémillard, and E. Luke, 2011b: Cloud radar Doppler spectra in drizzling stratiform clouds: 2. Observations and microphysical modeling of drizzle evolution. *J. Geophys. Res.*, **116**, D13203, https://doi.org/10.1029/2010JD015238.

——, and Coauthors, 2016: Development and applications of ARM millimeter-wavelength cloud radars. *The Atmospheric Radiation Measurement (ARM) Program: The First 20 Years*, *Meteor. Monogr.*, No. 57, Amer. Meteor. Soc., https://doi.org/10.1175/AMSMONOGRAPHS-D-15-0037.1.

——, B. Puigdomènech Treserras, and A. Protat, 2019: Calibration of the 2007–2017 record of Atmospheric Radiation Measurements cloud radar observations using CloudSat. *Atmos. Meas. Tech.*, **12**, 4949–4964, https://doi.org/10.5194/amt-12-4949-2019.

——, and Coauthors, 2020: The ARM radar network: At the leading edge of cloud and precipitation observations. *Bull. Amer. Meteor. Soc.*, **101**, E588–E607, https://doi.org/10.1175/BAMS-D-18-0288.1.

Krueger, S. K., C.-W. Su, and P. A. McMurtry, 1997: Modeling entrainment and finescale mixing in cumulus clouds. *J. Atmos. Sci.*, **54**, 2697–2712, https://doi.org/10.1175/1520-0469(1997)054<2697:MEAFMI>2.0.CO;2.

Kumjian, M. R., S. A. Rutledge, R. M. Rasmussen, P. C. Kennedy, and M. Dixon, 2014: High-resolution polarimetric radar observations of snow-generating cells. *J. Appl. Meteor. Climatol.*, **53**, 1636–1658, https://doi.org/10.1175/JAMC-D-13-0312.1.

Lamer, K., and P. Kollias, 2015: Observations of fair-weather cumuli over land: Dynamical factors controlling cloud size and cover. *Geophys. Res. Lett.*, **42**, 8693–8701, https://doi.org/10.1002/2015GL064534.

——, ——, and L. Nuijens, 2015: Observations of the variability of shallow trade wind cumulus cloudiness and mass flux. *J. Geophys. Res. Atmos.*, **120**, 6161–6178, https://doi.org/10.1002/2014JD022950.

Lawrence, M. G., 2005: The relationship between relative humidity and the dewpoint temperature in moist air: A simple conversion and applications. *Bull. Amer. Meteor. Soc.*, **86**, 225–234, https://doi.org/10.1175/BAMS-86-2-225.

Leahy, L. V., R. Wood, R. J. Charlson, C. A. Hostetler, R. R. Rogers, M. A. Vaughan, and D. M. Winker, 2012: On the nature and extent of optically thin marine low clouds. *J. Geophys. Res.*, **117**, D22201, https://doi.org/10.1029/2012JD017929.

Liu, Z., and Coauthors, 2009: The *CALIPSO* lidar cloud and aerosol discrimination: Version 2 algorithm and initial assessment of performance. *J. Atmos. Oceanic Technol.*, **26**, 1198–1213, https://doi.org/10.1175/2009JTECHA1229.1.

Unauthenticated | Downloaded 06/03/25 05:57 PM UTC

Luke, E. P., and P. Kollias, 2013: Separating cloud and drizzle radar moments during precipitation onset using Doppler Spectra. *J. Atmos. Oceanic Technol.*, **30**, 1656–1671, https://doi.org/10.1175/JTECH-D-11-00195.1.

——, F. Yang, P. Kollias, A. M. Vogelmann, and M. Maahn, 2021: New insights into ice multiplication using remote-sensing observations of slightly supercooled mixed-phase clouds in the Arctic. *Proc. Natl. Acad. Sci. USA*, **118**, e2021387118, https://doi.org/10.1073/pnas.2021387118.

Magaritz-Ronen, L., M. Pinsky, and A. Khain, 2016: Drizzle formation in stratocumulus clouds: Effects of turbulent mixing. *Atmos. Chem. Phys.*, **16**, 1849–1862, https://doi.org/10.5194/acp-16-1849-2016.

Martucci, G., C. Milroy, and C. D. O'Dowd, 2010: Detection of cloud-base height using Jenoptik CHM15K and Vaisala CL31 ceilometers. *J. Atmos. Oceanic Technol.*, **27**, 305–318, https://doi.org/10.1175/2009JTECHA1326.1.

Mather, J. H., and Voyles, J. W., 2013: The ARM Climate Research Facility: A review of structure and capabilities. *Bull. Amer. Meteor. Soc.*, **94**, 377–392, https://doi.org/10.1175/BAMS-D-11-00218.1.

Mead, J. B., and A. L. Pazmany, 2019: Quadratic phase coding for high duty cycle radar operation. *J. Atmos. Oceanic Technol.*, **36**, 957–969, https://doi.org/10.1175/JTECH-D-18-0108.1.

Mellado, J. P., 2017: Cloud-top entrainment in stratocumulus clouds. *Annu. Rev. Fluid Mech.*, **49**, 145–169, https://doi.org/10.1146/annurev-fluid-010816-060231.

Moeng, C.-H., B. Stevens, and P. P. Sullivan, 2005: Where is the interface of the stratocumulus-topped PBL? *J. Atmos. Sci.*, **62**, 2626–2631, https://doi.org/10.1175/JAS3470.1.

O'Connor, E. J., R. J. Hogan, and A. J. Illingworth, 2005: Retrieving stratocumulus drizzle parameters using Doppler radar and lidar. *J. Appl. Meteor.*, **44**, 14–27, https://doi.org/10.1175/JAM-2181.1.

Paluch, I. R., and D. G. Baumgardner, 1989: Entrainment and fine-scale mixing in a continental convective cloud. *J. Atmos. Sci.*, **46**, 261–278, https://doi.org/10.1175/1520-0469(1989)046<0261:EAFSMI>2.0.CO;2.

Pazmany, A. L., and S. J. Haimov, 2018: Coherent power measurements with a compact airborne Ka-band precipitation radar. *J. Atmos. Oceanic Technol.*, **35**, 3–20, https://doi.org/10.1175/JTECH-D-17-0058.1.

Pinsky, M., and A. Khain, 2019: Theoretical analysis of the entrainment–mixing process at cloud boundaries. Part II: Motion of cloud interface. *J. Atmos. Sci.*, **76**, 2599–2616, https://doi.org/10.1175/JAS-D-18-0314.1.

Prabhakaran, P., A. S. M. Shawon, G. Kinney, S. Thomas, W. Cantrell, and R. A. Shaw, 2020: The role of turbulent fluctuations in aerosol activation and cloud formation. *Proc. Natl. Acad. Sci. USA*, **117**, 16831–16838, https://doi.org/10.1073/pnas.2006426117.

Prenni, A. J., M. D. Petters, S. M. Kreidenweis, P. J. DeMott, and P. J. Ziemann, 2007: Cloud droplet activation of secondary organic aerosol. *J. Geophys. Res.*, **112**, D10223, https://doi.org/10.1029/2006JD007963.

Rauber, R. M., and Coauthors, 2015: The role of cloud-top generating cells and boundary layer circulations in the finescale radar structure of a winter cyclone over the Great Lakes. *Mon. Wea. Rev.*, **143**, 2291–2318, https://doi.org/10.1175/MWR-D-14-00350.1.

——, and Coauthors, 2017: Finescale structure of a snowstorm over the northeastern United States: A first look at high-resolution HIAPER cloud radar observations. *Bull. Amer. Meteor. Soc.*, **98**, 253–269, https://doi.org/10.1175/BAMS-D-15-00180.1.

Richards, M. A., 2014: *Fundamentals of Radar Signal Processing.* McGraw-Hill Education, 618 pp.

Romps, D. M., 2017: Exact expression for the lifting condensation level. *J. Atmos. Sci.*, **74**, 3891–3900, https://doi.org/10.1175/JAS-D-17-0102.1.

Sakradzija, M., and C. Hohenegger, 2017: What determines the distribution of shallow convective mass flux through a cloud base? *J. Atmos. Sci.*, **74**, 2615–2632, https://doi.org/10.1175/JAS-D-16-0326.1.

Sassen, K., 1991: The polarization lidar technique for cloud research: A review and current assessment. *Bull. Amer. Meteor. Soc.*, **72**, 1848–1866, https://doi.org/10.1175/1520-0477(1991)072<1848:TPLTFC>2.0.CO;2.

Schmidt, J., A. Ansmann, J. Bühl, and U. Wandinger, 2015: Strong aerosol–cloud interaction in altocumulus during updraft periods: Lidar observations over central Europe. *Atmos. Chem. Phys.*, **15**, 10687–10700, https://doi.org/10.5194/acp-15-10687-2015.

Shaw, R. A., 2003: Particle-turbulence interactions in atmospheric clouds. *Annu. Rev. Fluid Mech.*, **35**, 183–227, https://doi.org/10.1146/annurev.fluid.35.101101.161125.

——, and Coauthors, 2020: Cloud–aerosol–turbulence interactions: Science priorities and concepts for a large-scale laboratory facility. *Bull. Amer. Meteor. Soc.*, **101**, E1026–E1035, https://doi.org/10.1175/BAMS-D-20-0009.1.

Shupe, M. D., P. Kollias, S. Y. Matrosov, and T. L. Schneider, 2004: Deriving mixed-phase cloud properties from Doppler radar spectra. *J. Atmos. Oceanic Technol.*, **21**, 660–670, https://doi.org/10.1175/1520-0426(2004)021<0660:DMCPFD>2.0.CO;2.

Small, J. D., and P. Y. Chuang, 2008: New observations of precipitation initiation in warm cumulus clouds. *J. Atmos. Sci.*, **65**, 2972–2982, https://doi.org/10.1175/2008JAS2600.1.

Snider, J. R., D. Leon, and Z. Wang, 2017: Droplet concentration and spectral broadening in southeast Pacific stratocumulus clouds. *J. Atmos. Sci.*, **74**, 719–749, https://doi.org/10.1175/JAS-D-16-0043.1.

Stephens, G., D. Winker, J. Pelon, C. Trepte, D. Vane, C. Yuhas, T. L'Ecuyer, and M. Lebsock, 2018: *CloudSat* and *CALIPSO* within the A-Train: Ten years of actively observing the Earth system. *Bull. Amer. Meteor. Soc.*, **99**, 569–581, https://doi.org/10.1175/BAMS-D-16-0324.1.

Suzuki, K., J.-C. Golaz, and G. L. Stephens, 2013: Evaluating cloud tuning in a climate model with satellite observations. *Geophys. Res. Lett.*, **40**, 4464–4468, https://doi.org/10.1002/grl.50874.

Turner, D. D., and Coauthors, 2007: Thin liquid water clouds: Their importance and our challenge. *Bull. Amer. Meteor. Soc.*, **88**, 177–190, https://doi.org/10.1175/BAMS-88-2-177.

Vivekanandan, J., V. P. Ghate, J. B. Jensen, S. M. Ellis, and M. C. Schwartz, 2020: A technique for estimating liquid droplet diameter and liquid water content in stratocumulus clouds using radar and lidar measurements. *J. Atmos. Oceanic Technol.*, **37**, 2145–2161, https://doi.org/10.1175/JTECH-D-19-0092.1.

Vogl, T., M. Maahn, S. Kneifel, W. Schimmel, D. Moisseev, and H. Kalesse-Los, 2022: Using artificial neural networks to predict riming from Doppler cloud radar observations. *Atmos. Meas. Tech.*, **15**, 365–381, https://doi.org/10.5194/amt-15-365-2022.

Wang, J., Y.-N. Lee, P. H. Daum, J. Jayne, and M. L. Alexander, 2008: Effects of aerosol organics on cloud condensation nucleus (CCN) concentration and first indirect aerosol effect. *Atmos. Chem. Phys.*, **8**, 6325–6339, https://doi.org/10.5194/acp-8-6325-2008.

——, and Coauthors, 2022: Aerosol and Cloud Experiments in the Eastern North Atlantic (ACE-ENA). *Bull. Amer. Meteor. Soc.*, **103**, E619–E641, https://doi.org/10.1175/BAMS-D-19-0220.1.

Wang, L.-P., and W. W. Grabowski, 2009: The role of air turbulence in warm rain initiation. *Atmos. Sci. Lett.*, **10**, 1–8, https://doi.org/10.1002/asl.210.

Wang, Y., C. Zhao, Z. Dong, Z. Li, S. Hu, T. Chen, F. Tao, and Y. Wang, 2018: Improved retrieval of cloud base heights from ceilometer using a non-standard instrument method. *Atmos. Res.*, **202**, 148–155, https://doi.org/10.1016/j.atmosres.2017.11.021.

——, and Coauthors, 2020: Microphysical properties of generating cells over the Southern Ocean: Results from SOCRATES. *J. Geophys. Res. Atmos.*, **125**, e2019JD032237, https://doi.org/10.1029/2019JD032237.

Wang, Z., and K. Sassen, 2001: Cloud type and macrophysical property retrieval using multiple remote sensors. *J. Appl. Meteor.*, **40**, 1665–1682, https://doi.org/10.1175/1520-0450(2001)040<1665:CTAMPR>2.0.CO;2.

——, and Coauthors, 2009: Wyoming Cloud Lidar: Instrument description and applications. *Opt. Express*, **17**, 13576–13587, https://doi.org/10.1364/OE.17.013576.

Unauthenticated | Downloaded 06/03/25 05:57 PM UTC

Warner, J., 1973: The microstructure of cumulus cloud: Part IV. The effect on the droplet spectrum of mixing between cloud and environment. *J. Atmos. Sci.*, **30**, 256–261, https://doi.org/10.1175/1520-0469(1973)030<0256:TMOCCP>2.0.CO;2.

Wolfensberger, D., D. Scipion, and A. Berne, 2016: Detection and characterization of the melting layer based on polarimetric radar scans. *Quart. J. Roy. Meteor. Soc.*, **142**, 108–124, https://doi.org/10.1002/qj.2672.

Wood, R., 2012: Stratocumulus clouds. *Mon. Wea. Rev.*, **140**, 2373–2423, https://doi.org/10.1175/MWR-D-11-00121.1.

Yamaguchi, T., and D. A. Randall, 2012: Cooling of entrained parcels in a large-eddy simulation. *J. Atmos. Sci.*, **69**, 1118–1136, https://doi.org/10.1175/JAS-D-11-080.1.

Yang, F., E. P. Luke, P. Kollias, A. B. Kostinski, and A. M. Vogelmann, 2018: Scaling of drizzle virga depth with cloud thickness for marine stratocumulus clouds. *Geophys. Res. Lett.*, **45**, 3746–3753, https://doi.org/10.1029/2018GL077145.

——, F. Hoffmann, R. A. Shaw, M. Ovchinnikov, and A. M. Vogelmann, 2023a: An intercomparison of large-eddy simulations of a convection cloud chamber using haze-capable bin and Lagrangian cloud microphysics schemes. *J. Adv. Model. Earth Syst.*, **15**, e2022MS003270, https://doi.org/10.1029/2022MS003270.

——, and Coauthors, 2023b: A time-gated, time-correlated single-photon-counting lidar to observe atmospheric clouds at submeter resolution. *Remote Sens.*, **15**, 1500, https://doi.org/10.3390/rs15061500.

——, and Coauthors, 2024: A single-photon lidar observes atmospheric clouds at decimeter scales: Resolving droplet activation within cloud base. *npj Climate Atmos. Sci.*, **7**, 92, https://doi.org/10.1038/s41612-024-00644-y.

Yau, M. K., and R. R. Rogers, 1996: *A Short Course in Cloud Physics.* Elsevier, 304 pp.

Zhu, T., and D.-L. Zhang, 2006: Numerical simulation of Hurricane Bonnie (1998). Part II: Sensitivity to varying cloud microphysical processes. *J. Atmos. Sci.*, **63**, 109–126, https://doi.org/10.1175/JAS3599.1.

Zhu, Z., K. Lamer, P. Kollias, and E. E. Clothiaux, 2019: The vertical structure of liquid water content in shallow clouds as retrieved from dual-wavelength radar observations. *J. Geophys. Res. Atmos.*, **124**, 14184–14197, https://doi.org/10.1029/2019JD031188.

——, P. Kollias, E. Luke, and F. Yang, 2022: New insights on the prevalence of drizzle in marine stratocumulus clouds based on a machine learning algorithm applied to radar Doppler spectra. *Atmos. Chem. Phys.*, **22**, 7405–7416, https://doi.org/10.5194/acp-22-7405-2022.

——, ——, and F. Yang, 2023: Particle inertia effects on radar Doppler spectra simulation. *Atmos. Meas. Tech.*, **16**, 3727–3737, https://doi.org/10.5194/amt-16-3727-2023.

——, F. Yang, E. Luke, E. Rosky, K. Lamer, and P. Kollias, 2024: THz radar observations of hydrometeors in a spray chamber. *Geophys. Res. Lett.*, **51**, e2024GL109627, https://doi.org/10.1029/2024GL109627.

Unauthenticated | Downloaded 06/03/25 05:57 PM UTC